Please, cite as: Ricci, R., Romagnoli, R., Montelpare, S., Vitali, D., “Experimental study on a Savonius wind rotor for street lighting systems”, Applied Energy, 2016, 161, pp. 143–152
doi: https://doi.org/10.1016/j.apenergy.2015.10.012

Experimental study on a Savonius wind rotor for street lighting systems☆

Renato Ricci[a], Roberto Romagnoli[a,*], Sergio Montelpare[b], Daniele Vitali[a]

[a]*Department of Industrial Engineering and Mathematical Sciences (DIISM) University "Politecnica delle Marche", via Brecce Bianche 1, 60131 Ancona (Italy)*
[b]*Department of Engineering and Geology (INGEO), University of Chieti-Pescara, viale Pindaro 42, Pescara (Italy)*

Abstract

This paper investigates the aerodynamic performance of a Savonius vertical axis wind rotor to be used in an innovative lamppost. The wind generator studied is the main part of a public lighting system (a street lamp) powered by both aeolian and solar renewable energy sources. This study is aimed to analyze the effects of different construction solutions on rotor performance. Experimental dynamic tests were carried out on a 1:1 rotor model in the Environmental Wind Tunnel (EWT) of University "Politecnica delle Marche" (UNIVPM); tests were performed at different wind velocities and for different construction combinations. The results obtained confirmed that,in the tested range $2 - 3.3 \times 10^5$, rotor performance does not depend on the Reynolds number. Tests also showed that the presence of end plates and blade overlap increases the power coefficient $C_{P,max}$, while the presence of external grids and structural posts has negative effects on rotor performance. The best results were obtained for a configuration having a helical rotor with a 105°twist, open blade overlap and end plates.

Keywords: wind tunnel, experimental measurements, Savonius rotor, wind energy, street lamp, renewable Energies

1. Introduction

The last decades have been characterized by a growing interest in environmental issues and consequently in energy topics. Several researchers have dedicated their attention to study alternative energy production sources highlighting that the use of renewable energies and smart energy production systems can effectively contribute to the reduction of environmental impact and to greater energy efficiency. Following this line, a smart lamppost powered by renewable energy sources was developed at University "Politecnica delle Marche" (UNIVPM): the basic idea was to develop a system to be used in urban environments, in network or standalone configurations. The street light proposed is powered by both solar and wind energy: the

☆This document is a collaborative effort.

*Corresponding Author
Email addresses: ricci@univpm.it (Renato Ricci), r.romagnoli@univpm.it; roberto.r73@gmail.com (Roberto Romagnoli), s.montelpare@unich.it (Sergio Montelpare), d.vitali@univpm.it (Daniele Vitali)

Nomenclature

A	rotor swept area $[m^2]$
A_t	total frontal area (rotor + frame) $[m^2]$
a	overlap distance between buckets $[m]$
c	bucket chord $[m]$
C_P	power coefficient
C_T	torque coefficient
C_{TS}	static torque coefficient
D	rotor diameter (D = 2R) $[m]$
D_{ep}	end plate diameter $[m]$
d	shaft diameter $[m]$
H	turbine height $[m]$
l	lever arm length $[m]$
P	power $[W]$
R	rotor radius $[m]$
Re	Reynolds number
s	spacing distance between buckets$[m]$
S	test section area $[m^2]$
T	torque $[Nm]$
v_∞	free stream velocity $[ms^1]$
v	reduced section velocity $[m/s]$

Greek symbols

ϵ	blockage factor
λ	tip speed ratio
λ_c	tip speed ratio at witch $C_{P,max}$ occurs
ν	air kinematic viscosity
σ	standard deviation
ω	angular velocity $[rad/s]$
θ	position angle $[^o]$

Subscripts

max	maximum value

former is supplied by a photovoltaic panel placed on the upper end of the lamppost, the latter by three vertical axis wind rotors (VAWT) inserted, in line, along the support structure (Figure 1). The concept of using different energy sources derived from the aim to design a standalone system able to have several days of self-sufficiency and the consideration that on a windy day the sky is normally expected to be cloudy and photovoltaic production low, while on a sunny day wind velocities are expected to be low and so is aeolian production. By combining both energy sources the potentiality of a standalone system could be extended [1].

The choice to use a Savonius wind rotor derived from several positive considerations: it is very simple to build, economic, compact and has low noise emissions. Besides, it works with turbulent and fluctuating wind conditions typical of urban environments, it has a high static torque (self-starting wind turbine), it requires little maintenance and could be easily integrated into the design of vertical structures. On the other hand the power performance of a Savonius rotor is lower than that of a three blade horizontal axis wind turbine, therefore it is not suitable for significant energy production. Many authors have studied the Savonius wind rotor, obtaining maximum power coefficients in the range 0.10 - 0.25. As just mentioned, these are low values if compared to those obtained with other types of wind generators [2, 3]; this reason has led to a large number of numerical and experimental works analyzing the factors that could improve the rotor's performance. This

Figure 1: The UNIVPM prototype of the experimental street lamp powered by renewable sources.

is also the aim of this paper, since not all variables have been fully investigated and several divergences can be found in literature. Moreover, the Savonius rotor here investigated was designed to be implemented inside a street lamp and, due to practical construction choices, different geometric parameters had to be used, some of which were not present in literature. For these reasons, experimental tests were necessary in order to evaluate the influence of geometric and construction parameters on the rotor's performance. Experimental measurements were carried out in the Environmental Wind Tunnel (EWT) of UNIVPM. Tests were executed in dynamic conditions on a 1:1 scale model; the rotor twist, the presence of end plates, the effects of blade overlap and the presence of support posts were analyzed. The results are here illustrated in terms of $C_P - \lambda$ and $C_T - \lambda$ plots for all the different combinations of the tested elements.

2. Savonius rotor

The wind rotor selected is named after the Finnish engineer S.J. Savonius, the owner of its first patent, which dates back to 1930s [4, 5]. It is a vertical axis wind rotor with a simple geometry. In its most common shape it is made of two semi-cylindrical blades, asymmetrically positioned with respect to the vertical axis of rotation. Motion is generated by unbalanced aerodynamic forces acting on the advancing bucket, which is hit by the flow on its concave side, and the returning bucket, which moves in the opposite direction of the air flow. The concurrent force system produces a resultant moment along the rotational axis of the rotor which makes the system rotate. Due to its simple geometry, the Savonius rotor was also used as a water turbine with a horizontal axis configuration [6, 7]. According to literature, its geometry can be described by a few parameters which are illustrated in Figure 2. The Savonius turbine is classified as a drag device because the main forces acting on the blades are related to the aerodynamic pressure drag, but a well-designed rotor

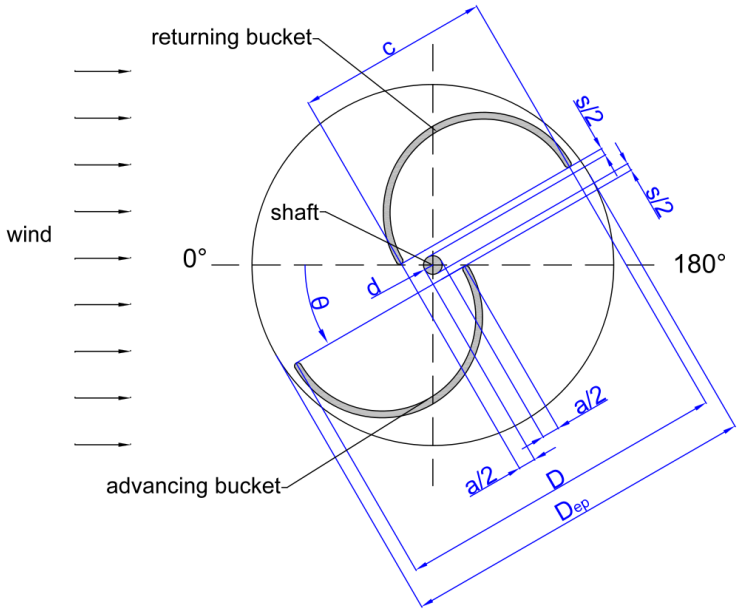

Figure 2: Schematic representation of a classic Savonius rotor section.

can reach tip speed ratios λ higher than 1.0 (eq. (3)); this result indicates rotational speeds higher than the inlet wind velocity and this is possible only if the rotor has also a lift behavior.

The first investigations available in literature were experimental studies with flow visualizations [8–11] or experimental tests aimed to measure the rotor's average performance in terms of static torque and power coefficient [12]. At a later stage many studies tried to analyze the rotor by measuring the surface pressure distribution over a single blade (e.g. [13–18]). In the same period a first numerical approach using the discrete vortex method to evaluate the flow field of a Savonius rotor was introduced [19–21]. In recent years several authors have used new techniques, such as P.I.V. [22] or C.F.D. (e.g. [23–27]), in order to analyze the fluid dynamic flow field, while others have focused their attention on techniques able to maximize the rotor's performance [6, 28–32].

Despite this large number of studies, many authors have reached contrasting conclusions on the role of the geometrical parameters of the rotor.

For example, several authors have positively evaluated the presence of an "open overlap" [12, 17, 18, 21, 33] and have agreed in suggesting an optimum overlap ratio between 10 and 15%. In these conditions it is possible to observe a jet flow through the overlap that increases the pressure on the concave side of the returning blade, thus reducing the overall drag [23]. Conversely, other authors negatively evaluate the presence of an open overlap if applied to slightly modified geometries [14, 34].

A general agreement can be observed in literature on the periodic behavior of the torque angular distribution, with a periodicity equal to the number of rotor blades [34, 35]. Measurements of the static torque

at different rotor angular positions have revealed significant variations; it is possible to observe both high positive values, which are useful to start the rotor, and negative values, which can give starting problems at certain wind angles. Besides, these oscillations may cause unpleasant cyclic stresses to the structure [36]. Such problems can be overcome by employing rotors with a higher number of blades, with staggered stages [36–39], or alternatively by using blades that are twisted along their vertical axis. However, also in this case different opinions can be found in literature: for example, [40, 41] have observed that the twist or the addition of stages increases the maximum C_P of the rotor, while others like [35] have obtained opposite results.

Likewise, also the analyses of the fluid dynamic parameters have often led to conflicting results: some authors assert that the Reynolds number affects both the power coefficient [39, 42] and the static torque coefficient (C_{TS}) [35], according to others it affects only C_{TS} [12], others still claim that it has no influence over the rotor's performance because they relate the differences to the friction of the bearings used in the experimental set-up [14].

Further information on the results of the experimental analyses performed on these and many other parameters can be found in [43], where the authors offer an extensive and accurate review of the experimental literature on Savonius rotors.

The wind turbine investigated in this work is the "classic" Savonius rotor with circular blades; its geometric characteristics are illustrated in 3.2. For this kind of rotor many authors (e.g. [12, 18, 36, 44]) have suggested an optimal configuration whose characteristics are shown in Table 1. Several of these parameters were adopted for the Savonius rotor tested in this paper, while others were modified (Table 2) in order to: facilitate industrial production (like for example the choice to use multiple rotor stages rather than twisted blades), improve structural stiffness (for example by modifying the central shaft diameter and the overlap ratio) and favor integration inside the lamppost (for example by increasing the aspect ratio).

Optimal solution			
number of buckets	2	helical step	0°/m
overlap ratio (a/c)	10-15 %	shaft presence	no
spacing ratio (s/c)	0	number of stages	2
aspect ratio (H/D)	1-1.2	angle between stages	90°
bucket arc angle	180°	$C_{P,max}$ (1 stage)	≃0.24
end plates D_{ep}/D	1.1	$C_{P,max}$ (2 stages)	≃0.28

Table 1: Optimal configuration for a Savonius rotor with semi-circular blades.

3. Experimental apparatus

3.1. The Environmental Wind Tunnel (EWT)

The EWT is a closed circuit wind tunnel as shown in Figure 3. The test section has a cross square area of 3.16 m^2 and is subdivided into three main subsections: the first subsection is used for aerodynamic tests requiring uniform velocity distribution and low turbulence levels. The second one is used to measure the effects of reciprocal interferences between slender bodies. The third one, the environmental section, is used to test wind effects over buildings, structures and orography models that are immersed into fully developed environmental boundary layers. The wind tunnel is equipped with a fan having a constant rotational speed

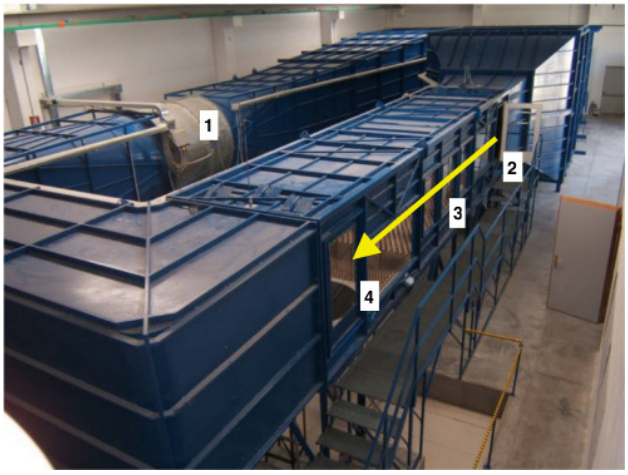

Figure 3: The Environmental Wind Tunnel of the University "Politecnica delle Marche": 1-fan 2-first test subsection 3-second test subsection 4-third test subsection.

of 975 RPM and 16 blades with an adjustable pitch. The average wind speed inside the test section ranges between 6 m/s and 40 m/s. Measurements carried out with a Constant Temperature Hot Wire Anemometer (CTA HWA) have shown a 2-D inlet speed uniformity within 2.5% and a turbulence intensity lower than 0.3%. The wind tunnel is also equipped with a compact heat exchanger that is used to limit temperature fluctuations within a range of 1 ℃.

3.2. The rotor models

The rotors presented in this research work are Savonius type turbines with semi-circular blades; they are built in a 1:1 scale with respect to those designed for the street lamp. The models have a diameter D of 0.384 m and are 1 m high. The section swept by the rotor is therefore of 0.384 m^2, while the blockage factor, introduced by [45] and defined in eq. (1), is 3.2 %. Considering also the experimental set-up support structure (fixed frame), the total blockage area reaches a maximum of 6.1 %. According to eq. (2), introduced

in [45], a correction coefficient was applied to the inlet velocity so as to take the blockage effect into account:

$$\epsilon = \frac{A_t}{4S} \tag{1}$$

$$v = v_\infty(1+\epsilon) \tag{2}$$

The rotor is composed of modular elements axially connected along a central shaft having a diameter d of 37 mm, so as to form a "skeleton". Such elements can be aligned or staggered by regular angles with respect to the vertical axis. In this way it is possible to build a rotor having a straight or a twisted geometry (i.e. an helical rotor). Three rotors were analyzed in this work (Figure 4): two helical rotors with overall twists of 90° and 105° respectively and a straight rotor (0°). The 105° twist was a technical specification limit fixed by the industrial partners appointed to build the final prototype. The surfaces of the rotor blades were made with a polyethylene sheet stretched upon the skeleton assembled; this polymeric material made it possible to follow the double curvature given by the twist. The sheet was fixed to the modular ribs and stretched so as to have a solid and regular surface for the flow. The rotor central shaft and the blade tips did not touch, rather they formed a gap of 18 mm allowing the flow to pass through.

Referring to Figure 2, the geometric characteristics of the rotors tested are summarized in Table 2.

Adopted solution			
number of buckets	2	helical step	0-90-105°/m
overlap ratio (a/c)	8.2 %	shaft diameter (d)	37 [mm]
spacing ratio (s/c)	0	number of stages	1
aspect ratio (H/D)	2.6	bucket arc angle	180°
end plates D_{ep}/D	no / 1.1	rotor diameter (D)	384 [mm]

Table 2: Geometric parameters of the rotors tested.

By comparing these parameters with those in Table 1, it is possible to observe that the design choices required a different geometry from the optimal one. Also for this reason, it was necessary to perform an experimental analysis to accurately determine the role of the modified construction parameters: i.e. end plates, helical step and central gap. Another parameter tested was the presence of poles placed externally to the rotor to support the lamppost; the project of the street lamp, in fact, included four steel tubular posts designed to assure the lamppost's structural resistance. In this way in the end application the helical rotors do not have to support the weight of the structure and therefore lighter materials can be used.

4. Measurement setup and procedure

In order to obtain C_P and C_T vs. λ curves for all the configurations tested, both wind speed and rotor angular velocity should be varied. Wind speed could be changed by adjusting the wind tunnel inlet flow

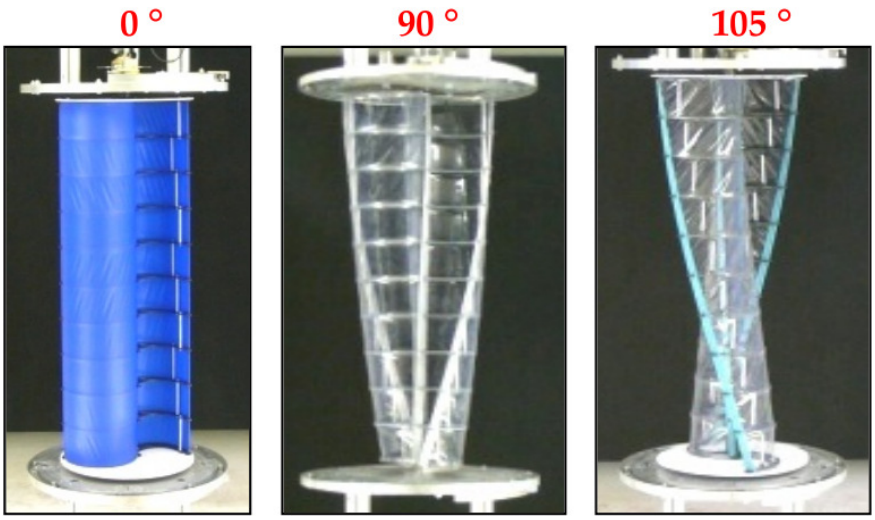

Figure 4: The rotors tested in the present work

velocity. The rotor angular velocity was varied by a hydraulic brake that clamped a disk coupled to the rotor shaft (Figure 5) and changed the counteracting torque; in the real case this action is performed by the torque of the electric generator coupled to the Savonius rotor. The testing procedure followed for this work was organized in the following steps: first of all a desired wind speed was selected, then the hydraulic brake was modulated on all its braking range, from null to full. In this way the system stabilized at different equilibrium states between the driving forces (fluid dynamics actions) and the resistant torque (braking friction loads) and it was possible to obtain enough operational points to draw the rotor characteristic curves.

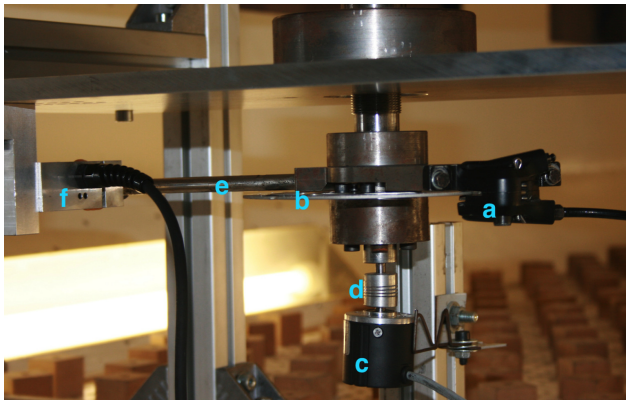

Figure 5: Details of the experimental apparatus: a) brake caliper b) break disk c) encoder d) joint e) lever arm f) load cell

Torque and power coefficients C_T and C_P, as well as the λ tip speed ratio, were obtained by measuring the

torque T and the angular velocity ω at the same time, according to eq. (3)-(4).

$$C_T = \frac{T}{0.5\,\rho\,A\,R\,v^2} \qquad \lambda = \frac{2\pi\,R\,\omega}{60\,v} \tag{3}$$

$$C_P = \frac{P}{0.5\,\rho\,A\,v^3} = \lambda\,C_T \tag{4}$$

The measurement apparatus is illustrated in Figure 5. The angular velocity ω was directly acquired as RPMs by an incremental encoder. A radial lever arm integrated within the braking system transmitted the torque T to a mono-axial load cell fixed to the set-up frame. The load cell was calibrated before the tests, using sample weights. The torque was obtained from the simple relationship $T = F\,l$, where F is the force measured on the load cell and l the length of the lever arm.

Tests were performed at different inlet flow velocities; a National Instrument data acquisition system was used for a real-time analysis of the experiment. Data were collected with an acquisition period of 3 seconds and a sampling rate of 1024 Hz.

5. Evaluation of measurement uncertainties

Measured quantities are affected by several kind of uncertainty that are normally classified as type A or type B. Type A uncertainties arise from factors that cannot be kept under control or whose effect cannot be reasonably determined "a priori". They are usually associated with random fluctuations that occur during acquisitions. Given a population standard deviation σ of the N values read in a single acquisition, the mean value that can be extracted is subjected to an uncertainty given by eq. (5).

$$\sigma_{ave} = \frac{\sigma}{\sqrt{N}} \tag{5}$$

Type B uncertainties, instead, are already known or can be evaluated "a priori" on the basis of the possible sources of error. In the case in question the type B uncertainties identified were related to the calibration and accuracy of the sensors used. Type A uncertainties were evaluated by the least squares straight line method, while type B uncertainties were directly derived from the technical specifications of the instruments used. When this latter information was not available, a rectangular error distribution was assumed, which can match the standard deviation of a normal distribution by dividing the maximum error of the instrument by a factor $\sqrt{3}$. When none of the two error types includes the other, the uncertainty of the quantities directly measured is obtained according to eq. (6). For the derived quantities, the error propagation law was used (7).

$$\sigma = \sqrt{\sigma_A^2 + \sigma_B^2} \tag{6}$$

$$f = f(x, y) \quad \Longrightarrow \quad \sigma_f = \sqrt{\left(\frac{\partial f}{\partial x}\sigma_x\right)^2 + \left(\frac{\partial f}{\partial y}\sigma_y\right)^2} \tag{7}$$

A 95% confidence level, corresponding to an interval of $\pm 2\sigma$, was chosen in order to evaluate extended uncertainties. Experimental tests showed a σ mean value of 2.37% for uncertainties associated with the single acquisitions, while the error associated with the σ_{ave} average acquisition value was approximately 0.07%.

6. Experimental Results

Several combinations of the parameters to be investigated were tested in the experimental analyses. The different configurations are summarized in Table 3, where the corresponding reference codes are listed. Each

Test code	Helical step (°/m)	End Plates (E)	Posts (P)
0deg_nE_nP	0	no	no
0deg_yE_nP	0	yes	no
0deg_nE_yP	0	no	yes (4)
0deg_yE_yP	0	yes	yes (4)
90deg_nE_nP	90	no	no
90deg_yE_nP	90	yes	no
90deg_nE_yP	90	no	yes (4)
90deg_yE_yP	90	yes	yes (4)
90deg_yE_yP3	90	yes	yes (3)
105deg_nE_nP	105	no	no
105deg_yE_nP	105	yes	no
105deg_nE_yP	105	no	yes (4)
105deg_yE_yP	105	yes	yes (4)

Table 3: Legend of the main configurations tested.

of the listed configurations was tested in dynamic conditions at different wind velocities v. The T, P vs $\omega(rpm)$ curves as well as the curves of the C_T and C_P vs λ coefficients were extracted.

6.1. Effect of the Reynolds number

As previously mentioned, researchers do not agree on the role of the Reynolds number on the performance of Savonius turbines. Some claim a Reynolds number dependency, while others assert that the different values of torque and power coefficients observed, obtained at different Re, are related to the friction of the bearings. Although in this work frictions were not directly measured, a comparison using two different experimental layouts was carried out: the first layout (I) was equipped with small bearings (SKF 4205ATN9, internal

diameter 25 mm, external diameter 52 mm, and SKF 6304, internal diameter 20 mm, external diameter 52 mm), the second layout (II) was assembled with considerably oversized bearings (SKF 5306, internal diameter 30 mm, external diameter 72 mm, and SKF 6008, internal diameter 40 mm, external diameter 68 mm). The comparison was made using a rotor with no twist, no end-plates, no posts and with an open overlap (0deg_nE_nP). The results obtained are shown in Figure 6 and Figure 7, while velocities and Reynolds numbers are illustrated in Table 4.

air speed v_∞	corrected speed v	Re number (I)	Re number (II)
6.9	7.3	–	199'940
7.7	8.1	–	221'851
8.5	9	–	246'501
9.1	9.6	249'629	–
11	11.6	301'635	–
12	12.7	330'238	–

Table 4: Velocities and Re numbers for the tests of Figure 6 and 7.

The Reynolds number was calculated according to eq. (8). The dynamic viscosity ν was calculated using the air temperature measured with a properly calibrated RTD PT100.

$$Re = \frac{v\,D}{\nu} \tag{8}$$

Both tests showed identical trends, although the curves obtained with the first assembly (test I) show a small reciprocal divergence at different velocities. The tests with the big bearings (II) were carried out at lower velocities to enhance the relative weight of bearing friction, but the curves perfectly overlap. This indicates that C_P and C_T are independent of the inlet flow velocities selected and, therefore, of the Reynolds number. It is thus plausible to affirm that the discrepancies observed in the tests with small bearings are due to the greater mechanical friction effects. By regressing the experimental data with a least squares third order polynomial curve it is possible to obtain $C_{P,max} = 0.189$ at $\lambda = 0.67$ for test (I) and $C_{P,max} = 0.192$ at $\lambda = 0.65$ for test (II); i.e. the differences are negligible.

6.2. Effect of the end plates

End plates are built in the form of circular discs applied to both the ends of the rotor. Their effect is illustrated in Figure 8 for the straight rotor and in Figure 9(a) and 9(b) for the helical ones.

The graph points refer to the experimental values obtained at different wind velocities, while the fitting curve was obtained from a least squares third order polynomial regression on all the data acquired. An improvement effect due to the confinement of the flow inside the rotor can be observed, which confirms the

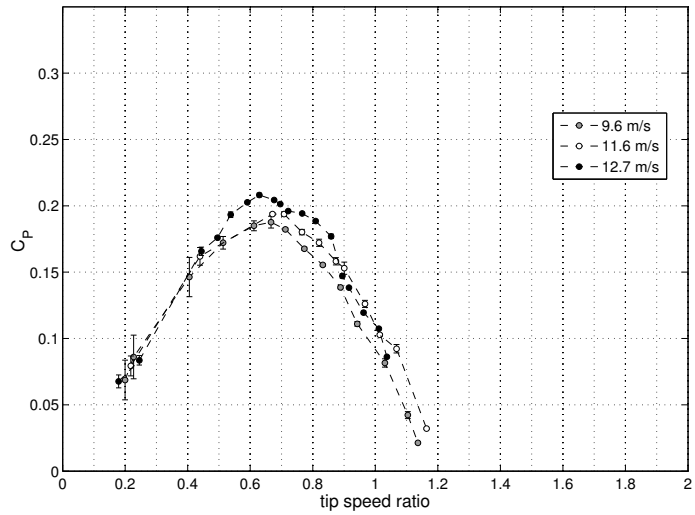

(a) set-up with the small bearings (test I)

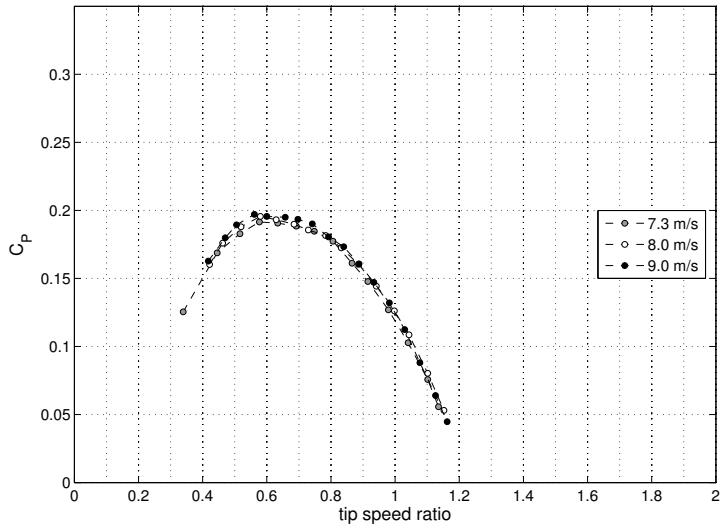

(b) set-up with the big bearings (test II)

Figure 6: Effect of the Re number on the C_P curves.

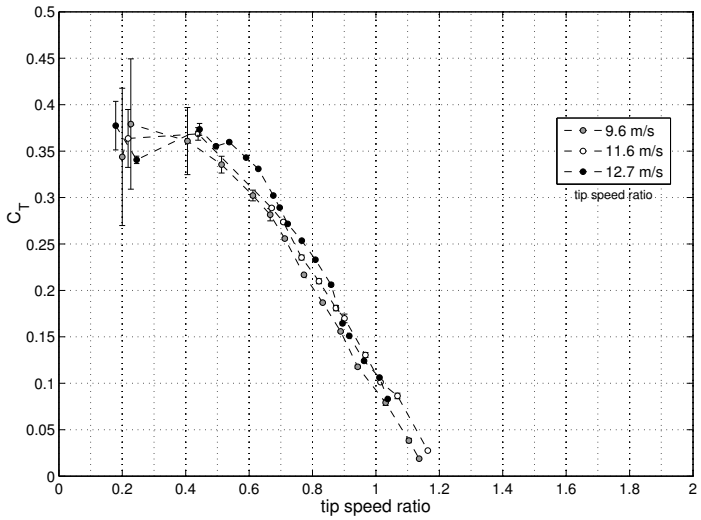

(a) set-up with the small bearings (test I)

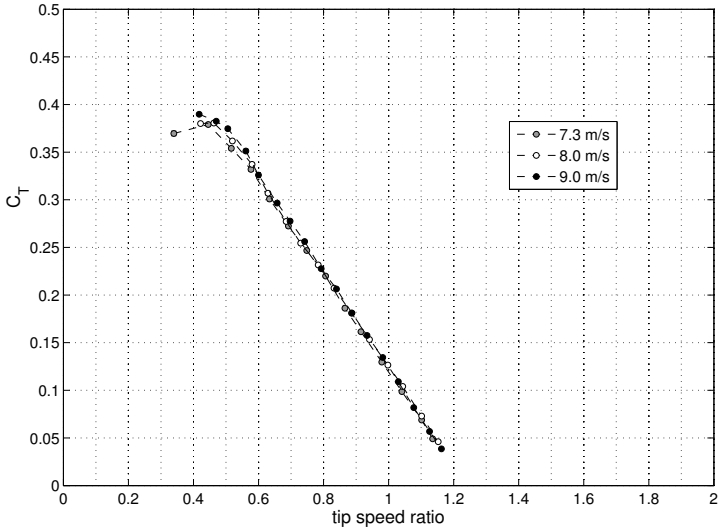

(b) set-up with the big bearings (test II)

Figure 7: Effect of the Re number on the C_T curves.

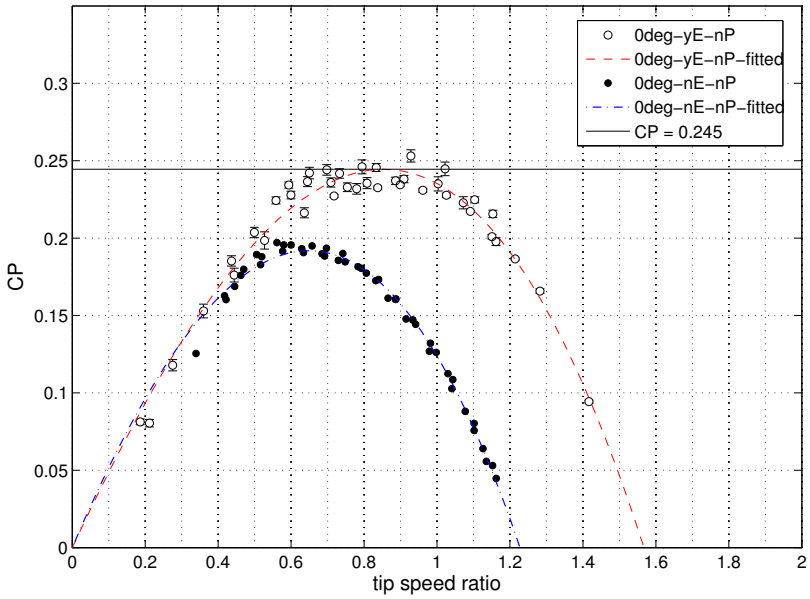

Figure 8: Effect of the end plates (rotor with no helical step).

results illustrated in literature. In the present case, the improvement of the peak of C_P, as calculated from the fitting curve, is between 27% and 39% (refer to Table 5). In order to simplify the comparison among the different configurations, a horizontal line, corresponding to the maximum C_P of a reference test, is shown in the graphs. This reference is the straight rotor with end-plates (0deg_yE_nP), which corresponds to the most frequent configuration observed in literature.

Helical step (°)	0	90	105
without end plates	0.192	0.172	0.18
with end plates	0.245	0.226	**0.251**
variation	+27 %	+31 %	**+39 %**

Table 5: $C_{P,max}$ in the configuration with end plates.

6.3. Effect of the helical step

The effect of the helical twist can again be deduced from Table 5, while the results for the rotors with end plates are illustrated in Figure 10. It can be noticed that for a configuration with end plates, which resulted to be the best choice, the rotor with a step of 90° has a slightly lower $C_{P,max}$ with respect to the one with a twist of 105°; in absence of end plates, the helical step causes lower performance due to the augmented flow escape.

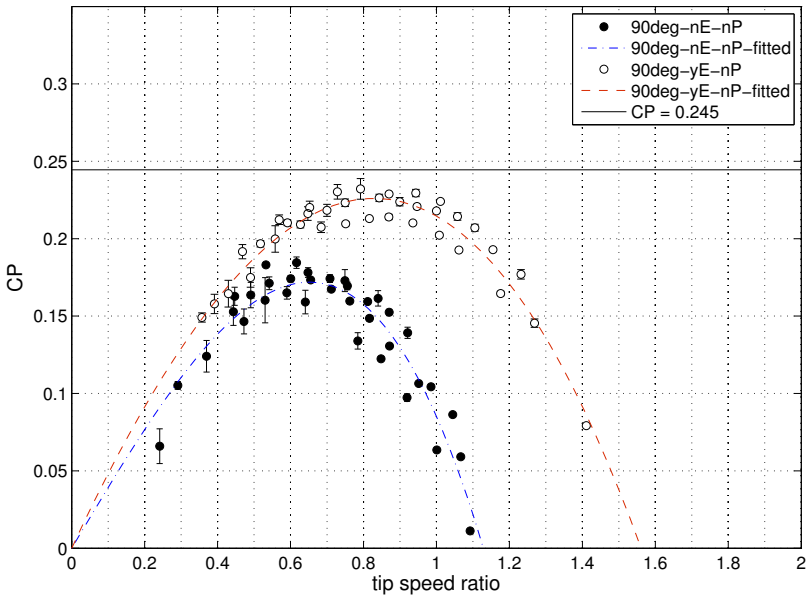

(a) Rotor with 90°/m helical step.

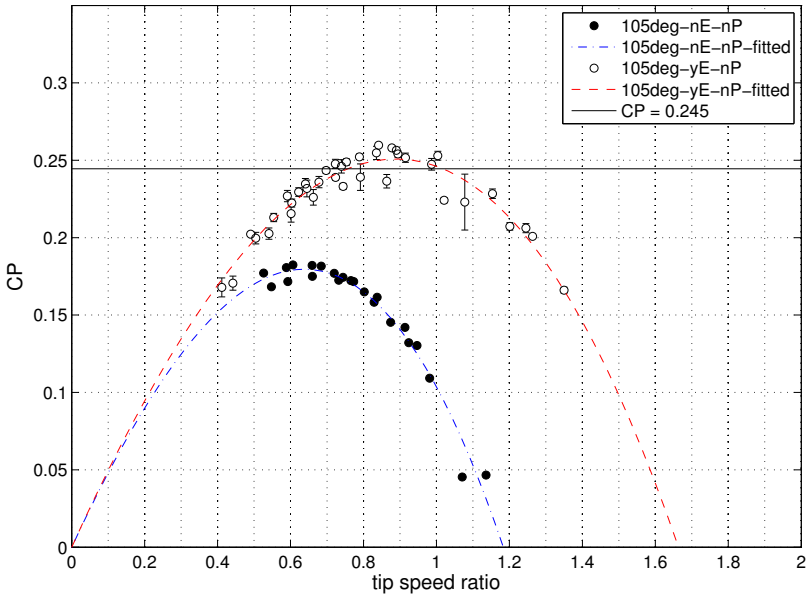

(b) Rotor with 105°/m helical step.

Figure 9: Effect of the end plates on helical rotor efficiency C_P.

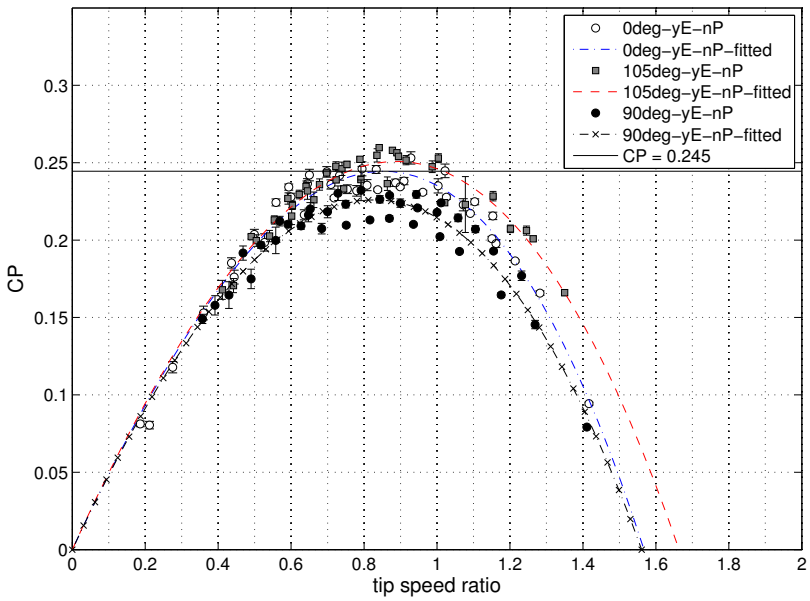

Figure 10: Effect of helical step on rotor efficiency C_P (rotors with End Plates).

6.4. Effect of the posts

The posts are built as vertical cylindrical poles with a diameter of 42 *mm* and provide a structural support to the street lamp. They are placed externally at a distance of 635 *mm* from the center of the rotor and are arranged at every 90°. Experimental tests were performed with the orientation reported in Figure 11 in order to evaluate their greatest disturbance effect. Tests were performed by using both the

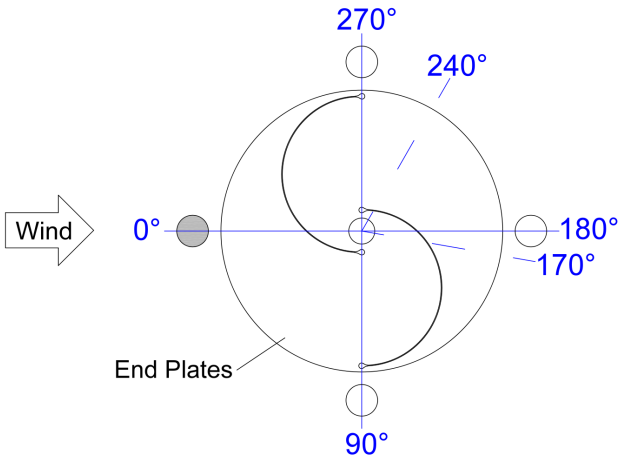

Figure 11: Position of the posts and angular references used. In the tests with three posts the grey element was removed.

three and four post configurations. When measuring the configuration with three posts, the post upstream the rotor was removed (the circle filled in grey in Figure 11). The results of these tests are illustrated in

Table 6 and in Figure 12, 13(a) and 13(b); as expected, it is possible to observe a significant decrease in performance in the configuration with four posts and a less evident effect in the case with three posts. This can be explained in two ways:

- the post upstream the rotor causes disturbance to the incident flow (leeward wake, flow deviation and overpressure on the incoming blade);
- the other posts cause only overpressures on the blades approaching them.

This last item allows to explain the lower decrease in performance observed in the tests with three posts illustrated in Figure 12 and Figure 13(a). Finally a difference in the effect of the posts depending on the twist can be observed : the rotor twisted by 90° seems to suffer from this phenomenon more than the others. The better behavior was experienced by the 105° due to the phase shift among the blade sections approaching the post.

Posts	Helical step (°/m)		
	0	90	105
no	0.245	0.226	**0.251**
3 posts	0.224 (-8.2 %)	0.195 (-13.7 %)	—
4 posts	0.187 (-23.4 %)	0.155 (-31.4 %)	0.206 (-17.9 %)

Table 6: $C_{P,max}$ with the presence of posts.

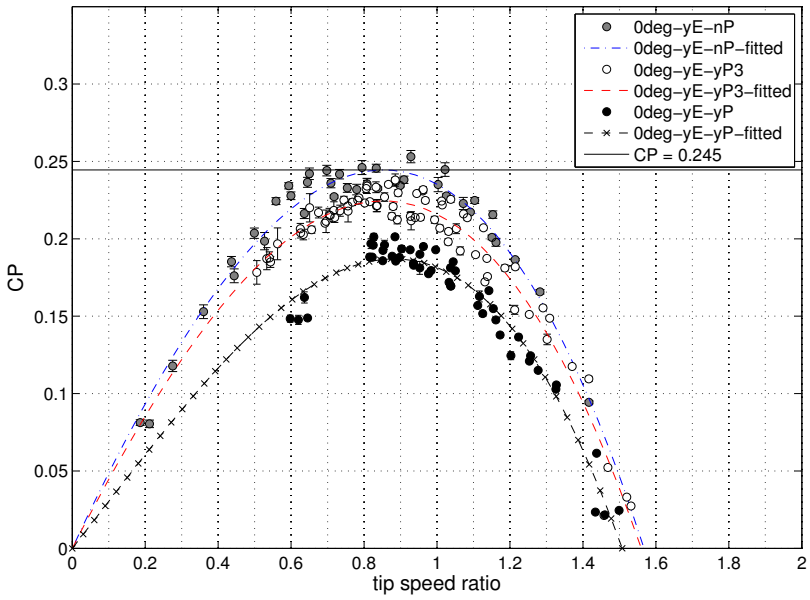

Figure 12: Effect of the posts on the rotor efficiency C_P.

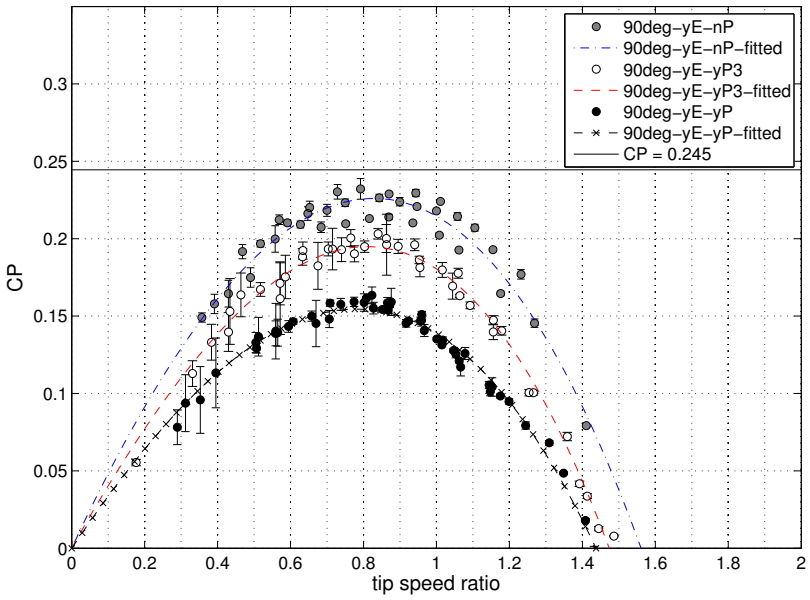

(a) Rotor with 90°helical step.

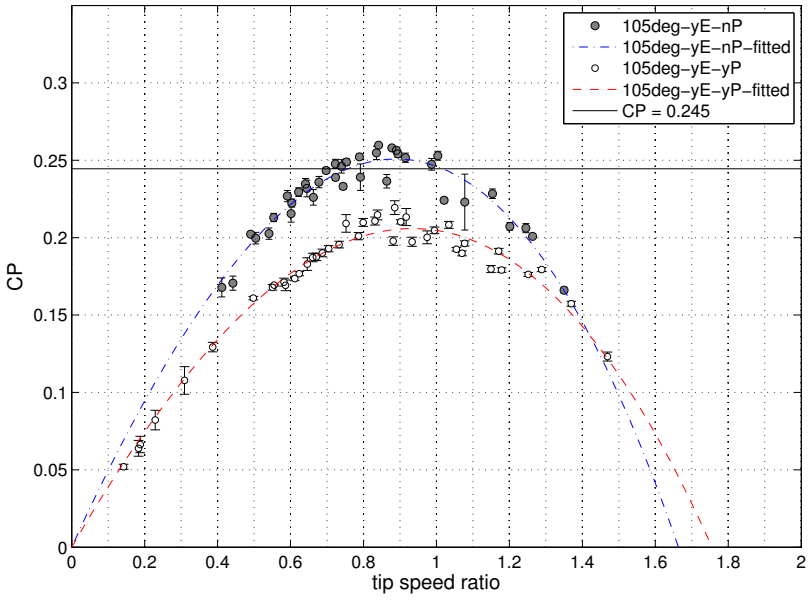

(b) Rotor with 105°helical step.

Figure 13: Effect of the posts on the helical rotor efficiency C_P.

6.5. External grid effect

An issue raised during the street lamp design process was the need to test some systems to protect the rotating parts from collisions with external objects. A simple solution is a wire mesh to be placed externally to the wind rotors. These grids provide an adequate mechanical protection but they also induce pressure drops in the flow: this could negatively affect the performance of the wind rotor by reducing the wind dynamic pressure available for conversion. In order to evaluate these effects, different configurations were tested using two different wire meshes with square openings: one with a square side length of 1 cm (a normal grid), the other with a side of 6 cm (a wider and lighter grid). The ratio between the total area and the mesh open area, defined as porosity, is 70% in the first case and 95% in the second. Tests were performed on the 105° helical rotor without end plates and the results obtained are shown in Figure 14. Experiments showed that rotor performance strongly decreases (-32 % on $C_{P,max}$) when placing a normal grid on the whole rotor circumference (black circles). So a gradual increase of the porosity was performed by lightening the normal grid in different positions (see Figure 14):

- in the front area (LGa, white circles);
- in the front and in the back areas (LGab, white triangles);
- on the side of the advancing bucket (LGc, blue triangles);
- on most part of the rotor (LGd, red square).

Finally a last configuration with no grids on the advancing bucket side (black square) was tested. The results show that all the solutions adopted reduce rotor performance in a similar way, but the worst solution is the configuration with the normal grid (black circles). The main numerical results are reported in Table 7.

Code	Light grid (LG)	Normal grid (G)	$C_{P,max}$
105deg_nE_nP	no	no	0.18
105deg_nE_yG	no	0°-360°	-32 %
105deg_nE_yG_LGa	0°-90°	elsewhere	-23 %
105deg_nE_yG_LGab	0°-90°, 170°-240°	elsewhere	-21 %
105deg_nE_yG_LGc	0°-180°	elsewhere	-18 %
105deg_nE_yG_LGd	0°-240°	elsewhere	-14 %
105deg_nE_yG180	no	180°-360°	-14 %

Table 7: Variation of $C_{P,max}$ when an external grid is present (see also Figure 11).

6.6. Effect of the overlap

The influence of the overlap was examined by closing the gap near the rotational axis with an insulating tape. The helical rotor with a twist of 105° was used to analyze the jet-flow effect. The results illustrated in Figure 15 show that the absence of the gap causes a decrease in $C_{P,max}$ by 17%.

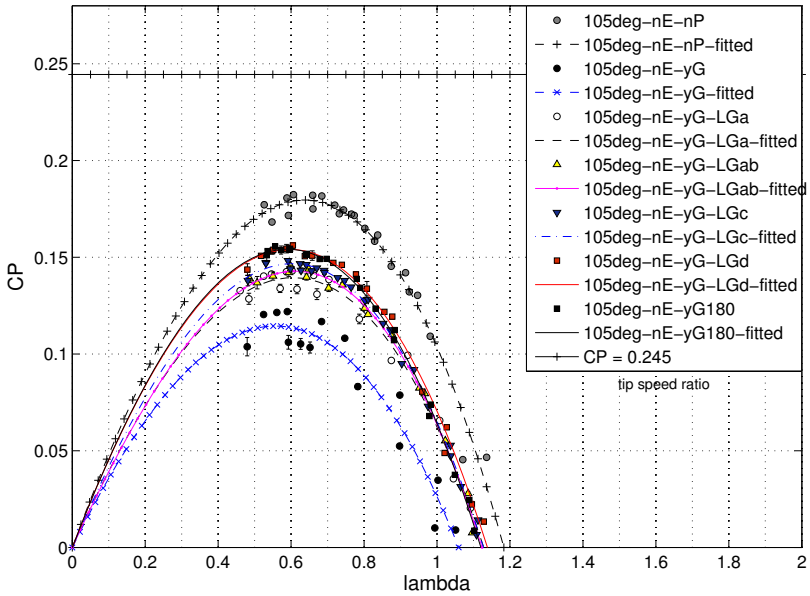

Figure 14: Grid effect (rotor with 105°h.s., no End Plates).

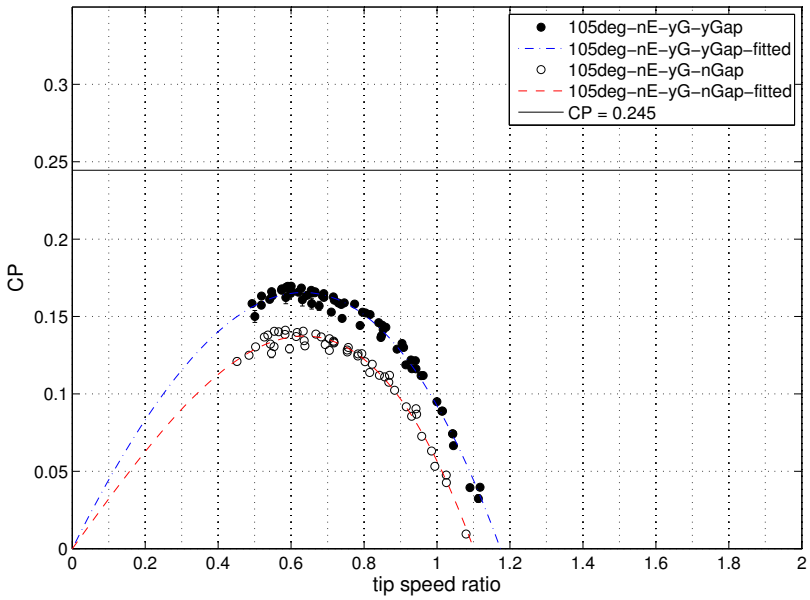

Figure 15: Open overlap effect (rotor with 105°h.s. and grid).

7. Concluding remarks

This article reports the results of experimental tests performed in a wind tunnel on a Savonius wind rotor to be used on a street lamp powered by renewable energy. Due to practical design requirements and architectural restrictions some non optimal choices were made in terms of the geometry of the Savonius rotor used compared to the optimal configuration suggested in literature (like, for example, the choice for a higher aspect ratio). As a consequence, the authors had to carry out new experimental analyses in order to redefine new optimal configurations and verify their performance. Tests were carried out to evaluate the influence on the rotor's performance of single or combined applications of: the Reynolds number, a helical step of 0, 90 and 105°, an open overlap, end plates and external pillar posts. The overall results of the tests performed are shown in Table 8.

Test code	Helical Step (°/m)	End Plates (E)	Posts (P)	Light grid (LG)	Normal grid (G)	$C_{P,max}$	λ_C	λ_{max}
0deg_nE_nP	0	no	no	no	no	0.192	0.649	1.16
0deg_yE_nP	0	yes	no	no	no	0.245	0.854	1.57
0deg_yE_yP	0	yes	yes (4)	no	no	0.187	0.882	1.51
0deg_yE_yP3	0	yes	yes (3)	no	no	0.224	0.853	1.56
90deg_nE_nP	90	no	no	no	no	0.172	0.652	1.13
90deg_yE_nP	90	yes	no	no	no	0.226	0.828	1.56
90deg_yE_yP	90	yes	yes (4)	no	no	0.155	0.781	1.44
90deg_yE_yP3	90	yes	yes (3)	no	no	0.195	0.809	1.47
105deg_nE_nP	105	no	no	no	no	0.180	0.637	1.18
105deg_yE_nP	105	yes	no	no	no	**0.251**	0.889	1.66
105deg_yE_yP	105	yes	yes (4)	no	no	0.206	0.934	1.76
105deg_nE_yG	105	yes	yes	no	0-360°	0.122	0.597	1.07
105deg_nE_yG_LGa	105	yes	yes	0-90°	elsewhere	0.139	0.605	1.13
105deg_nE_yG_LGab	105	yes	yes	0-90+170-240°	elsewhere	0.143	0.612	1.13
105deg_nE_yG_LGc	105	yes	yes	0-180°	elsewhere	0.147	0.603	1.13
105deg_nE_yG_LGd	105	yes	yes	0-240°	elsewhere	0.154	0.597	1.14
105deg_nE_yG180	105	yes	yes	no	180-360°	0.154	0.590	1.12

Table 8: Summary of the main experimental results.

Whereas the main findings of this study are summarized hereinafter:

- the tests were carried out for Reynolds numbers between 200000 and 330000: in this range the performance (C_P and C_T) was not dependent on the Reynolds number;
- the absence of the open overlap caused a decrease in the performance of $C_{P,max}$ by about 17%;
- the helical rotor achieved lower performance compared to the straight rotor with the 90° step (-6/7% of $C_{P,max}$), while a twist of 105 ° showed similar performance;

- the end plates always had an improving effect, which, however, was greater for the helical rotor with a step of 105° (+ 39% of $C_{P,max}$);
- the supporting posts negatively affected the performance due to two reasons:
  a) leeward wake;
  b) overpressure generated on the approaching blade;
- the negative effect of the posts, which can reach – 31.4% of $C_{P,max}$, was not the same for all rotors: the effect was smaller for the helical rotor with a step of 105° (-17.9%);
- external grids had a negative effect on the rotor's performance depending on the grid position and porosity;
- the best results were obtained for a helical rotor with a step of 105°, with end plates and open gap; in this condition a $C_{P,max}$ of 0.251 at $\lambda = 0.899$ was measured.

8. Acknowledgments

This work was performed thanks to the support of the projects IPA P.O.W.E.R.E.D (www.powered-ipa.it) and Ministry of Economic Development "INDUSTRIA 2015".

9. References

[1] R. Ricci, S. Montelpare, D. Vitali, An innovative wind–solar hybrid street light: development and early testing of a prototype, International Journal of Low-Carbon Technologies 0 (2014) 1–10.

[2] R. E. Wilson, P. B. Lissaman, Applied Aerodynamics of wind power machines, no. GI-41840 in Research Applied to National Needs, Oregon State University, 1974.

[3] A. Jha, Wind Turbine Technology, ISBN 13: 978-1-4398-1507-6, CRC Press, 2011.

[4] S. J. Savonius, The S-rotor and its applications, Mechanical Engineering 5 (53) (1931) 333–338.

[5] S. J. Savonius, The wing rotor in theory and practice, Savonius Co., 1928.

[6] K. Golecha, T. Eldho, S. Prabhu, Influence of the deflector plate on the performance of modified Savonius water turbine, Applied Energy (88) (2011) 3207–3217.

[7] M. Khan, G. Bhuyan, M. Iqbal, J. Quaicoe, Hydrokinetic energy conversion systems and assessment of horizontal and vertical axis turbines for river and tidal applications: A technology status review, Applied Energy (86) (2009) 1823–1835.

[8] G. von Bach, Untersuchungen fiber Savonius-rotoren und verwandte strömungsmaschinen, Forsh. Geb. Ing. 2 (1931) 218–231.

[9] G. Bergeles, N. Athanassiadis, On the flow field around a Savonius rotor, Wind Eng. 6 (1982) 140–148.

[10] G. J. Bowden, S. A. McAleese, The properties of isolated and coupled Savonius rotors, Wind Eng. 8 (1984) 271–288.

[11] J. Massons, J. Gavalda, X. Ruiz, F. Diaz, Image analysis of the wake generated by a Savonius rotor, Wind Eng. 12 (1988) 341–351.

[12] B. F. Blackwell, R. E. Sheldahl, L. V. Feltz, Wind tunnel performance data for two and three bucket Savonius rotors, United States Energy Research and Development Administration under contract AT .

[13] A. Chauvin, D. Benghrib, Drag and lift coefficients evolution of a Savonius rotor, Experiments in Fluids 8 (1989) 118–120.

[14] V. J. Modi, M. S. U. K. Fernando, On the performance of the Savonius wind turbine, Journal of Solar Energy Engineering 111 (1989) 71–81.

[15] V. J. Modi, M. S. U. K. Fernando, N. J. Roth, Aerodynamics of the savonius rotor: experiments and analysis, vol. 5, IECEC, Energy Conversion Engineering Conference. Proceedings of the 25th Intersociety, 213 – 218, 1990.

[16] M. Kotb, T. Aldoss, Flowfield around a partially-blocked Savonius rotor, Applied Energy 38 (2) (1991) 17–132.

[17] N. Fujisawa, F. Gotoh, Visualization study of the flow in and around a Savonius rotor, Experiments in Fluids (12) (1992) 407–412.

[18] N. Fujisawa, On the torque mechanism of Savonius rotors, Journal of Wind Engineering and Industrial Aerodynamics 40 (1992) 277–292.

[19] M. S. U. K. Fernando, V. J. Modi, A numerical analysis of the unsteady flow past a Savonius wind turbine, Journal of Wind Engineering and Industrial Aerodynamics (32) (1989) 303–327.

[20] V. J. Modi, M. S. U. K. Fernando, Unsteady aerodynamics and wake of the Savonius wind turbine: a numerical study, Journal of Wind Engineering and Industrial Aerodynamics 46-47 (1993) 811–816.

[21] N. Fujisawa, Velocity measurements and numerical calculations of flow fields in and around Savonius rotors, Journal of Wind Engineering and Industrial Aerodynamics 59 (1996) 39–50.

[22] A. Shigetomi, Y. Murai, Y. Tasaka, Y. Takeda, Interactive flow field around two Savonius turbines, Renewable Energy (2011) 536–545.

[23] V. D'Alessandro, S. Montelpare, R. Ricci, A. Secchiaroli, Unsteady Aerodynamics of a Savonius wind rotor: a new computational approach for the simulation of energy performance, Energy 35 (8) (2010) 3349–3363.

[24] S. Roy, U. K. Saha, Review on the numerical investigations into the design and development of Savonius wind rotors, Renewable and Sustainable Energy Reviews (23) (2013) 73–83.

[25] K. Kacprzak, G. Liskiewicz, K. Sobczak, Numerical investigation of conventional and modified Savonius wind turbines, Renewable Energy (60) (2013) 578–585.

[26] L. A. Danao, J. Edwards, O. Eboibi, R. Howell, A numerical investigation into the influence of unsteady wind on the performance and aerodynamics of a vertical axis wind turbine, Applied Energy (116) (2014) 111–124.

[27] M. Tartuferi, V. D'Alessandro, S. Montelpare, R. Ricci, Enhancement of Savonius wind rotor aerodynamic performance: a computational study of new blade shapes and curtain systems, Energy 79 (2015) 371–384.

[28] B. M. Shaughnessy, S. D. Probert, Partially-blocked savonius rotor, Applied Energy (43) (1992) 239–249.

[29] I. Dobrev, F. Massouh, CFD and PIV investigation of unsteady flow through Savonius wind turbine, Energy Procedia (2011) 711–720.

[30] B. Altan, M. Atilgan, The use of a curtain design to increase the performance level of a Savonius wind rotors, Renewable Energy 35 (4) (2010) 821–829.

[31] S. Rolland, M. Thatcher, W. Newton, A. Williams, T. Croft, D. Gethin, M. Cross, Benchmark experiments for simulations of a vertical axis wind turbine, Applied Energy (111) (2013) 1183–1194.

[32] S. Roy, U. K. Saha, Wind tunnel experiments of a newly developed two-bladed Savonius-style wind turbine, Applied Energy 137 (2015) 117–125.

[33] R. Ricci, S. Montelpare, G. Borrelli, V. D'Alessandro, Experimental Analysis of a Savonius Wind Rotor for Streetlighting Systems, in: Thermal and Environmental issue in energy systems, Sorrento, Italy, 603–607, 2010.

[34] M. A. Kamoji, S. B. Kedare, S. V. Prabhu, Experimental investigations on single stage modified Savonius rotor, Applied Energy 86 (7-8) (2009) 1064–1073.

[35] M. Kamoji, S. Kedare, S. Prabhu, Performance tests on helical Savonius rotors, Renewable Energy 34 (3) (2009) 521–529.

[36] T. Hayashi, Y. LI, Y. Hara, Wind tunnel tests on a different phase three-stage Savonius rotor, JSME International Journal 48 (1, series B).

[37] J. L. Menet, A double-step Savonius rotor for local production of electricity: a design study, Renewable Energy 29 (11) (2004) 1843–1862.

[38] N. Mahmoud, El-Haroun, E. Wahba, M. Nasef, An experimental study on improvement of Savonius rotor performance, Alexandria Engineering Journal (51) (2012) 19–25.

[39] J. Kumbernuss, J. Chen, H. Yang, L. Lu, Investigation into the relationship of the overlap ratio and shift angle of double stage three bladed vertical axis wind turbine (VAWT), Journal of Wind Engineering and Industrial Aerodynamics (107-108) (2012) 57–75.

[40] U. K. Saha, M. Rajkumar, On the performance analysis of Savonius rotor with twisted blades, Renewable Energy 31 (11) (2006) 1776–1788.

[41] U. K. Saha, S. Thotla, D. Maity, Optimum design configuration of Savonius rotor through wind tunnel experiments, Journal of Wind Engineering and Industrial Aerodynamics 96 (8-9) (2008) 1359–1375.

[42] A. Damak, Z. Driss, M. Abid, Experimental investigation of helical Savonius rotor with a twist of 180 °, Renewable Energy (52) (2013) 136–142.

[43] J. V. Akwa, H. A. Vielmo, A. P. Petry, A review on the performance of Savonius wind turbines, Renewable and Sustainable Energy Reviews 16 (5) (2012) 3054 – 3064, ISSN 1364-0321.

[44] M. Nakajima, S. Iio, T. Ikeda, Performance of double-step Savonius rotor for environmentally friendly hydraulic turbine, Journal of Fluid Science and Technology 3 (3) (2008) 410–419.

[45] A. Pope, J. B. Barlow, W. H. Rae, Low-Speed Wind Tunnel Testing, John Wiley & Sons, 3rd edn., 1999.